Aust. J. Phys., 1975, **28**, 557–74

Downhole Induced-polarization Detection of Ore Bodies: Conductive Overburden Effects

L. J. Gleeson and Y.-C. Thio

Faculty of Science, Monash University, Clayton, Vic. 3168.

Abstract

Highly conducting overburden layers inhibit the surface detection of ore bodies by induced polarization (IP) measurements. The excitation and response of an IP source obtained by means of underground (downhole) electrodes is investigated utilizing a simple model: the overburden is represented by a uniform surface layer and the ore body by a small sphere. The shielding of the source from the surface is shown. Quantitative estimates of the improvement obtained by siting the electrodes below the overburden–host-rock interface are obtained. It is expected that similar improvement will be obtained with larger ore bodies. It is shown that the improvement applies to time-domain and frequency-domain measurements. A feature of the results is the presence of a 'blind' zone just beneath the interface. The optimization of electrode positions in a particular geometry is examined.

1. Introduction

The use of induced polarization (IP) measurements in Australia to determine the presence of subterranean ore bodies is inhibited by the presence of an overburden layer which is of higher conductivity than the underlying host material containing the ore body (Gleeson and Thio 1973). The usual measurement procedure used is to place a pair of current electrodes on the surface to inject current into the system, and to place a second pair of potential electrodes also on the surface to pick up signals originating in the polarized ore body (e.g. Parasinis 1966).

By using a simple model we have shown (Gleeson and Thio 1973) that, under representative conditions (overburden ~ 100 times as conductive as host material), the signal potential from a small IP source is reduced by a factor of ~ 1000 when an overburden layer is present between the IP source and the surface. In this paper we again use a very simple model to examine quantitatively the advantages to be obtained by placing these electrode systems beneath the surface. In practical applications they would be placed down suitable bore holes.

In the model (Fig. 1) the overburden is represented by a layer of conductivity σ_1 with thickness h and the underlying material has conductivity σ_2. The ore body is represented by a small sphere of polarizable material situated at P_s, a depth b below the surface. The overburden is designated region 1 and the underlying part region 2. At position P_s the current density due to the excitation current is the vector $\boldsymbol{J}(P_s)$. Following Siegel (1959), the response of the ore body to this currrent density is represented by a current dipole at the centre of the sphere with the dipole moment p proportional to the excitation current density at that point, i.e.

$$p = -k\, J(P_s)\,.$$

The current dipole at P_s in turn produces signal voltages at the potential electrodes.

The analytical procedure is outlined in Section 2 and some representative current flow patterns and potential distributions are given. In Section 3 the current densities produced at a target by downhole current electrodes are determined and compared with those produced by surface electrodes in the absence of overburden. In Section 4 the downhole measurement of IP potentials is examined, and in Section 5 the maximization of excitation currents and signal potentials is studied and the concept of a 'blind' zone just below the interface emerges. Section 6 contains a discussion of two reciprocity relationships we have found useful and in Section 7 we show the relationship between time-domain and frequency-domain measurements. The principal results are discussed and our conclusions are noted in Section 8. As far as possible mathematical formulae and derivations have been put in appendices.

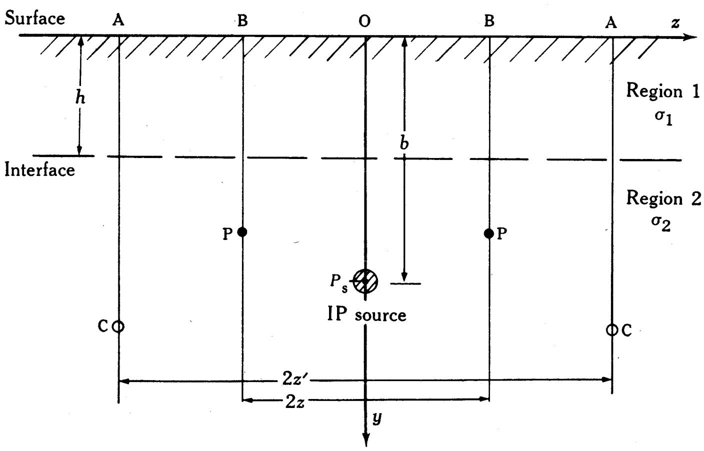

Fig. 1. Showing the planar geometry assumed, together with the current-electrode positions (C) in holes A and the potential-electrode positions (P) in holes B.

2. Method of Analysis

In this problem, Poisson's equation

$$\nabla . \{\sigma(x)\, \nabla\phi(x)\} = -i(x)$$

governs the potential $\phi(x)$ at a position x in a region of conductivity $\sigma(x)$ and in which $i(x)$ is the injected current per unit volume. The solution for a point current source of unit strength at position x' is the Green's function $G(x;x')$. It is well known that the reciprocity relationship

$$G(x;x') = G(x';x)$$

applies to these solutions (e.g. Morse and Feshbach 1953).

All of the formulae we require can be derived from the Green's function for a current monopole in a two-layer geometry. The potential ϕ due to a pair of current electrodes is then simply the sum of the potentials from monopoles delivering currents $+I$ and $-I$ respectively and the current density $\boldsymbol{J}$ is given by

$$\boldsymbol{J} = -\sigma\nabla\phi.$$

The potential due to a current dipole moment $\boldsymbol{p}$ is obtained by placing two monopoles of current $\pm I_{\rm d}$ at small separation $\boldsymbol{a}$ and having $\boldsymbol{p} = I_{\rm d}\,\boldsymbol{a}$.

The potential functions are given by equations (A1) of Appendix 1. In cartesian coordinates with origin at O in Fig. 1, the current density $\boldsymbol{J}(\boldsymbol{x};\boldsymbol{x}')$ at a point $\boldsymbol{x} = (x,y,z)$, due to a monopole of current strength I at a position $\boldsymbol{x}' = (x',y',z')$, is

$$\begin{aligned}\boldsymbol{J}(\boldsymbol{x};\boldsymbol{x}') = \frac{I}{4\pi}\Bigg(&\frac{(x-x')\boldsymbol{e}_x+(y-y')\boldsymbol{e}_y+(z-z')\boldsymbol{e}_z}{\{(x-x')^2+(y-y')^2+(z-z')^2\}^{3/2}}\\&-p_{12}\frac{(x-x')\boldsymbol{e}_x+(y+y'-2h)\boldsymbol{e}_y+(z-z')\boldsymbol{e}_z}{\{(x-x')^2+(y+y'-2h)^2+(z-z')^2\}^{3/2}}\\&+(1-p_{12}^2)\sum_{n=0}^{\infty}p_{12}^n\frac{(x-x')\boldsymbol{e}_x+(y+y'+2nh)\boldsymbol{e}_y+(z-z')\boldsymbol{e}_z}{\{(x-x')^2+(y+y'+2nh)^2+(z-z')^2\}^{3/2}}\Bigg),\end{aligned}\tag{1}$$

provided $\boldsymbol{x}$ and $\boldsymbol{x}'$ both lie below the interface. In equation (1) we have $p_{12} = (\sigma_1-\sigma_2)/(\sigma_1+\sigma_2)$ and $(\boldsymbol{e}_x,\boldsymbol{e}_y,\boldsymbol{e}_z)$ are unit vectors in the directions of the (x,y,z) axes. The corresponding expressions for other combinations of $\boldsymbol{x}$ and $\boldsymbol{x}'$ relative to the interface are given by equations (A3) of Appendix 1.

Figs 2*a* and 2*b* illustrate the current flow according to equation (1) when $s = \sigma_2/\sigma_1 = 0{\cdot}05$ with a single monopole. This value of s is typical of Australian conditions. Fig. 2*a* is for the case $y'/h = 0{\cdot}5$ and Fig. 2*b* for the case $y'/h = 2$. Fig. 2*c* shows the disposition with two electrodes separated horizontally by $2h$. The features to note in these figures are: (i) the horizontal stretching of the current lines in the upper layer when the electrode is in this layer, indicating shunting of current by this more conductive layer; and (ii) the bending of the lines toward the upper layer, suggesting a 'suction' effect of this layer on the current.

The potential at $\boldsymbol{x}$ due to a current dipole of moment $\boldsymbol{p}$ placed at $\boldsymbol{x}'$ is

$$\begin{aligned}\phi_{\rm d}(\boldsymbol{x};\boldsymbol{x}') = -\frac{\boldsymbol{p}}{4\pi\sigma_2}\cdot\Bigg(&\frac{(x'-x)\boldsymbol{e}_x+(y'-y)\boldsymbol{e}_y+(z'-z)\boldsymbol{e}_z}{\{(x'-x)^2+(y'-y)^2+(z'-z)^2\}^{3/2}}\\&-p_{12}\frac{(x'-x)\boldsymbol{e}_x+(y'+y-2h)\boldsymbol{e}_y+(z'-z)\boldsymbol{e}_z}{\{(x'-x)^2+(y'+y-2h)^2+(z'-z)^2\}^{3/2}}\\&+(1-p_{12}^2)\sum_{n=0}^{\infty}p_{12}^n\frac{(x'-x)\boldsymbol{e}_x+(y'+y+2nh)\boldsymbol{e}_y+(z'-z)\boldsymbol{e}_z}{\{(x'-x)^2+(y'+y+2nh)^2+(z'-z)^2\}^{3/2}}\Bigg),\end{aligned}\tag{2}$$

when $\boldsymbol{x}$ and $\boldsymbol{x}'$ are both in region 2; the other expressions are given by equation (A4) with equations (A3) of Appendix 1.

The potential distribution due to a dipole at depth $b = 2h$ and with $\boldsymbol{p}$ parallel to the surface is illustrated in Fig. 3*a* for $s = 0{\cdot}01$. This figure gives the potential pattern in a vertical plane including the vector $\boldsymbol{p}$ and the axis OO′ passes through the dipole. The pattern in a plane through OO′ making an angle ψ with the above

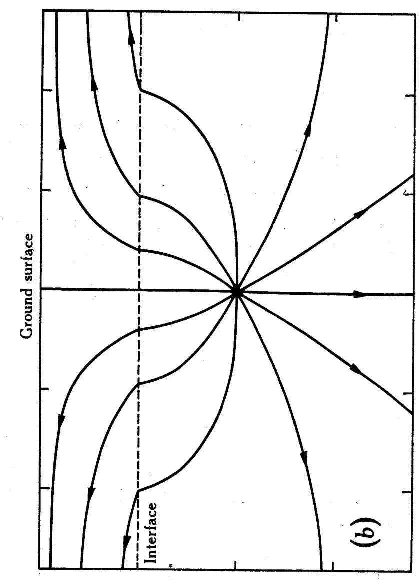

Fig. 2. Current lines for:
(*a*) a monopole placed in the overburden, under the conditions $s = \sigma_2/\sigma_1 = 0\cdot05$, $y'/h = 0\cdot5$;
(*b*) a monopole placed below the overburden, under the conditions $s = 0\cdot05$, $y'/h = 2$;
(*c*) a pair of current electrodes placed below the overburden, under the conditions $s = 0\cdot04$, $y'/h = 1\cdot5$.

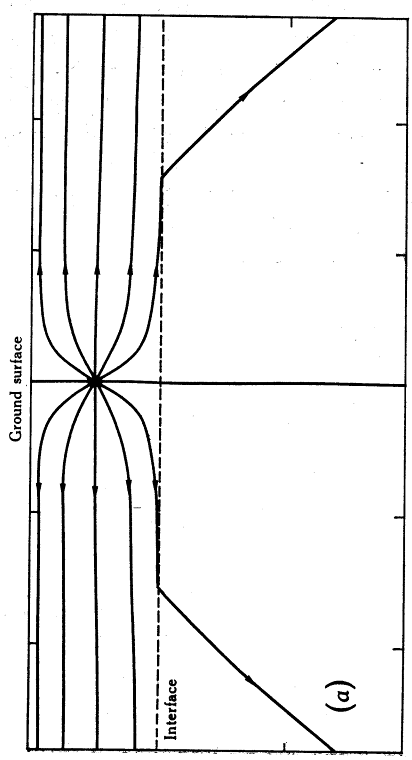

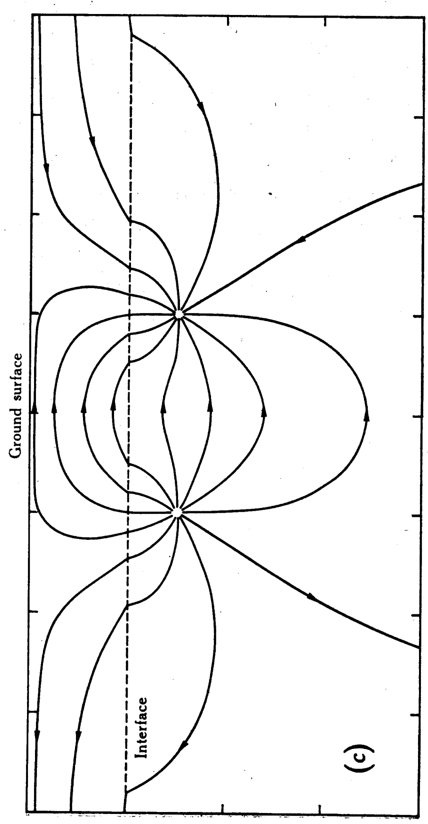

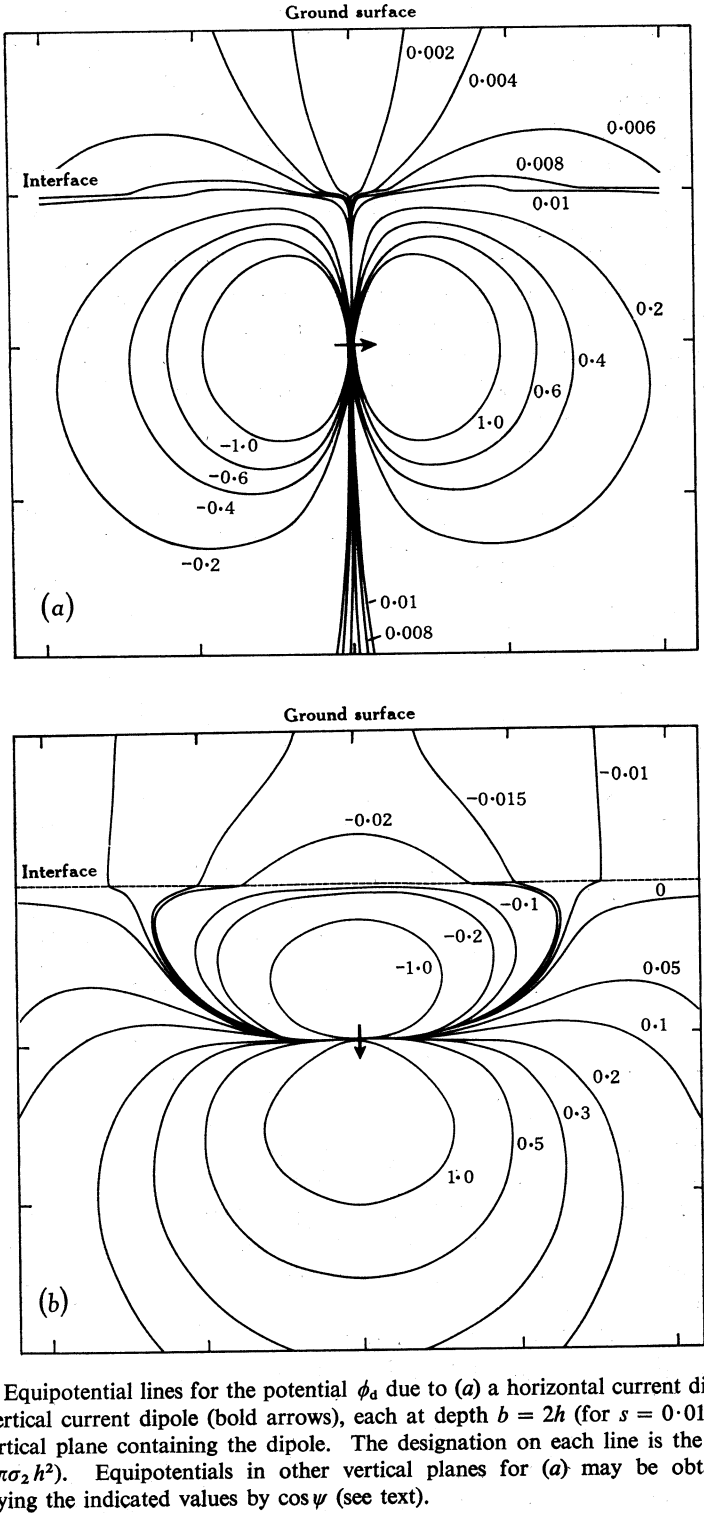

Fig. 3. Equipotential lines for the potential ϕ_d due to (*a*) a horizontal current dipole and (*b*) a vertical current dipole (bold arrows), each at depth $b = 2h$ (for $s = 0{\cdot}01$), shown in a vertical plane containing the dipole. The designation on each line is the value of $\phi_d/(p/4\pi\sigma_2 h^2)$. Equipotentials in other vertical planes for (*a*) may be obtained by multiplying the indicated values by $\cos\psi$ (see text).

plane is again that of Fig. 3*a* save that the potentials must be multiplied by $\cos\psi$. This result is obtained by resolving $\boldsymbol{p}$ into components $p\cos\psi$ and $p\sin\psi$ parallel and perpendicular to the plane and noting that the potential contribution from the latter is zero in the plane.

The potential map for a vertical dipole placed as above is given in Fig. 3*b*; this map is the same in all vertical planes through OO′. With Figs 3*a* and 3*b* we can obtain the potential at any point in the region due to any dipole at depth $2h$ by resolving its moment $\boldsymbol{p}$ into horizontal and vertical components.

The features of Figs 3*a* and 3*b* are the way in which the equipotentials spread in the upper layer, indicating a reduction in potential at a point on the surface. Corresponding to this spread is a concentration of equipotential lines just below the interface. This concentration indicates that there is a sharp reduction in potential as the interface is approached from below. Both of these aspects are examined more quantitatively in Section 4.

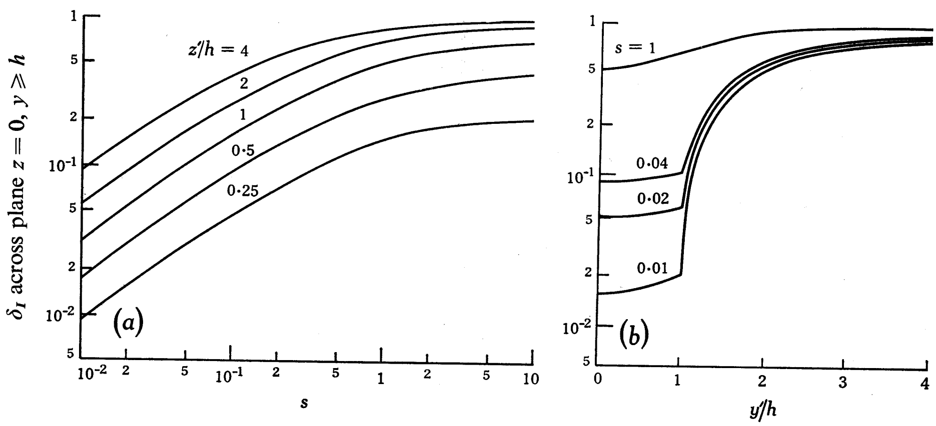

Fig. 4. Comparisons of the fraction δ_I of total current crossing the plane $z = 0$ below the interface ($y \geqslant h$) when the current electrodes are placed (*a*) on the surface and (*b*) downhole. In (*a*), δ_I is shown as a function of the conductivity contrast s for typical values of z'/h. In (*b*), δ_I is shown as a function of the depth y' of the electrodes for a range of s values when the electrode separation $2z' = 2h$.

3. Symmetrical Case: Current Electrode Variation

Since the possible combination of positions for current and potential electrodes is infinite, for definiteness we take the configuration displayed in Fig. 1. The current electrodes are assumed to be in holes A separated by $2z'$ and at the same depth y', while the target orebody is at a depth b midway between the current electrodes. The potential electrodes are placed in holes B and these too are symmetrically positioned with separation $2z$. Extensive calculations of current distributions, potentials and attenuation due to overburden layers for the case of *surface* electrodes have been given by Gleeson and Thio (1973).

The advantage to be gained by downhole placement of current electrodes is demonstrated in a broad way by Fig. 4. Fig. 4*a* is for current electrodes placed on the surface and it shows, as a function of s $(= \sigma_2/\sigma_1)$, the fraction δ_I of total current which crosses the plane $z = 0$ *below the interface*. This plane is midway between the current electrodes and perpendicular to the line joining them. Curves are plotted for several typical values of z'/h. We note that, for $s = 0{\cdot}01$ and for z' in the range $0{\cdot}25 \leqslant z'/h \leqslant 4$, reductions by a factor of ~ 10 relative to the homogeneous case ($s = 1$) are obtained.

Fig. 4*b* is for downhole current electrodes and shows the fraction δ_I of total current below the interface (i.e. in the lower layer) as a function of y'/h (electrode depth relative to overburden depth). The figure is drawn for the particular case $z'/h = 1$ and a range of s values. The percentage current below the interface should be compared in each case with that obtained with $s = 1$ and surface electrodes. We note that for $s \ll 1$, there is little if any gain until the electrodes are placed below the interface.

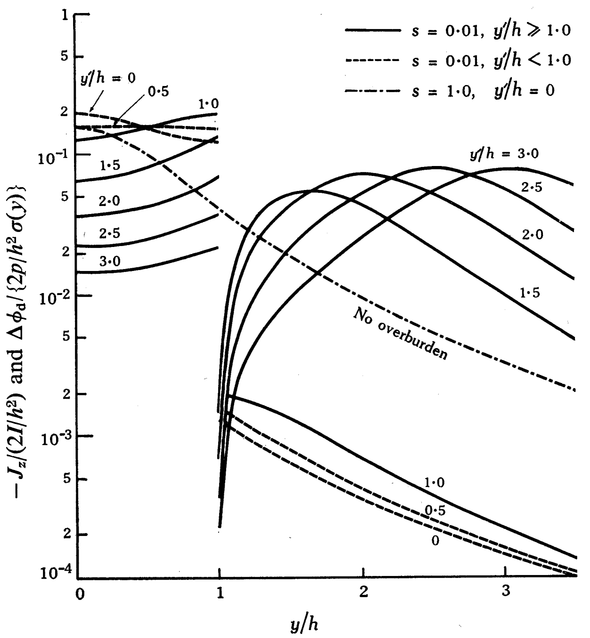

Fig. 5. Current density J_z as a function of depth on the y axis due to a pair of current electrodes at depth y' and separated by $2z'$ (see Fig. 1), in the case when $z'/h = 1$. The dot–dash curve shows the current density for surface electrodes and no overburden while the continuous and dashed curves are for electrodes below and above the interface respectively. The curves also give the potential $\Delta\phi_d$ divided by $2p/h^2\sigma(y)$ for downhole potential electrodes; in this case the parameters y'/h become b/h (see text).

We now turn to the detailed distribution of current, particularly that below the interface, produced with downhole current electrodes. The current density at a depth y on the y axis is given by $J_x = 0$, $J_y = 0$ and

$$J_z(y;y') = -\frac{Iz'}{2\pi}\left(\frac{1}{\{(y-y')^2+z'^2\}^{3/2}} - \frac{p_{12}}{\{(y+y'-2h)^2+z'^2\}^{3/2}} + (1-p_{12}^2)\sum_{n=0}^{\infty}\frac{p_{12}^n}{\{(y+y'+2nh)^2+z'^2\}^{3/2}}\right), \tag{3}$$

if both $y \geqslant h$ and $y' \geqslant h$. Expressions for other combinations of y and y' may be obtained from equations (A3) in Appendix 1.

Fig. 5 shows the current density at points on the y axis for the case $z'/h = 1$ and $s = 0{\cdot}01$. Curves are given for current electrode positions $y'/h = 0$–$3{\cdot}0$. The dot–dash curve represents the distribution for the case of electrodes placed on the surface of a homogeneous ground ($s = 1$). The increase in current density obtained by the downhole placement of the current electrodes is obvious, and at target depths well below the overburden it is possible to produce a current density greater than that with surface electrodes on a homogeneous ground. Note again that there is no improvement until the current sources are located below the interface. Note also the region just under the interface where the current density is low; we discuss this in detail in Section 5.

4. Downhole Potential Electrodes

Increased signals can also be obtained by placing the potential (i.e. pickup) electrodes in downhole positions. The potential map of Fig. 3*a* (or its equivalent in any particular case) can be used to evaluate the signal that may be obtained from electrodes placed in any position in the neighbourhood of the IP source. Thus, for example, it is clear by inspection of this figure that the potential difference obtained by siting the potential electrodes below the surface in the holes B of Fig. 1 first increases as the depth y increases, reaches a maximum, and then decreases. The variation of potential difference with other geometry for the probe positioning (e.g. oblique holes) can also be evaluated in this way.

Once again for definiteness, we evaluate the symmetrical case. The potential difference $\Delta\phi_{\mathrm{d}}$ between electrodes in the geometry of Fig. 1, with separation $2z$ and at depth y, due to an induced dipole of moment p at depth b is given by

$$\Delta\phi_{\mathrm{d}} = \frac{pz}{2\pi\sigma_2}\left(\frac{1}{\{(b-y)^2+z^2\}^{3/2}} - \frac{p_{12}}{\{(b+y-2h)^2+z^2\}^{3/2}} + (1-p_{12}^2)\sum_{n=0}^{\infty}\frac{p_{12}^n}{\{(b+y+2nh)^2+z^2\}^{3/2}}\right), \tag{4}$$

if both $y > h$ and $b > h$. Expressions for $\Delta\phi_{\mathrm{d}}$ in the other cases may be obtained from equation (A4) in Appendix 1. The relation (4) is the same in form as that for the current density on the y axis given by equation (3) except that z replaces z', $-p/\sigma_2$ replaces the current I from the current source, and the depth b of the dipole replaces the depth y' of the current electrodes.

Because the form of equation (4) is identical with that of (3), $\Delta\phi_{\mathrm{d}}$ has the same dependence on the depth y of the potential electrodes as J_z has dependence on the position along the y axis. Thus Fig. 5 also represents $\Delta\phi_{\mathrm{d}}$ versus electrode depth if the vertical ordinate is taken to be $\Delta\phi_{\mathrm{d}}/\{2p/h^2\sigma(y)\}$. The separate curves are for different dipole depths b/h so that $y'/h \to b/h$. Note that $\Delta\phi_{\mathrm{d}}$ is actually continuous across the interface; the discontinuity of the curves is introduced through the discontinuity of $\sigma(y)$ in $h^2\sigma(y)$, the scale factor of $\Delta\phi_{\mathrm{d}}$ in Fig. 5. If given in terms of a constant scale factor $p/h^2\sigma_2$, say, the curves of $\Delta\phi_{\mathrm{d}}$ would have the sections in the overburden region ($0 \leqslant y/h \leqslant 1$) dropped to join at the interface with those in the region $y/h > 1$. Thus with overburden, the conditions of Fig. 5 and a source below the interface ($b/h > 1$), the potential difference $\Delta\phi_{\mathrm{d}}$ decreases sharply as the interface is approached from below and remains at roughly the interface value as the potential electrodes move to the surface. We note particularly: (i) that the overburden reduces $\Delta\phi_{\mathrm{d}}$ at the surface very considerably, (ii) that potential electrodes must be placed below the interface in order to improve this value of $\Delta\phi_{\mathrm{d}}$ and (iii) that a major decrease in $\Delta\phi_{\mathrm{d}}$ occurs in a zone just below the interface.

5. Maximization and Envelope Curves

We turn now to the question of optimization of the current density at a given depth y on the y axis (where the target is assumed to be located) by means of variation of the depth of the current electrodes, i.e. by variation of y' in Fig. 5 and equation (3). The current density curves drawn in Fig. 5 represent the function $J_z(y;y')$ given explicitly by equation (3). We note particularly that

$$J_z(y;y') = J_z(y';y), \tag{5}$$

that is, y' and y may be interchanged in this function.

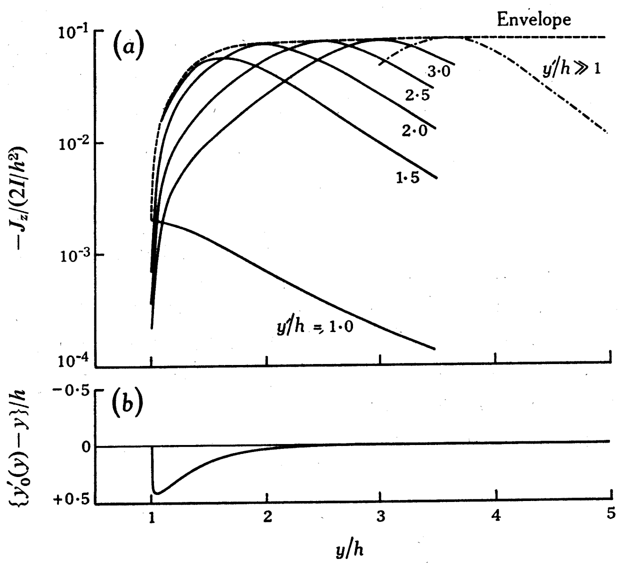

Fig. 6. Showing: (*a*) the current density curves of Fig. 5 for $y \geqslant h$ (with $s = 0{\cdot}01$, $z'/h = 1$) together with their envelope (dashed curve), and (*b*) the curve specifying the electrode positions $y_0'(y)$ which maximize the current density at depth y. The dot–dash curve in (*a*) gives the current density distribution for electrodes placed well below the interface.

In Fig. 6*a* we have reproduced the set of current density curves for $y \geqslant h$ and the fixed values of the current electrode depth y' of Fig. 5. We note that these curves have an envelope which each curve touches (the dashed curve of Fig. 6*a*). The maximum current density that can be obtained at depth y is given by the envelope value. In order to obtain this maximum current density, the current electrodes should be placed at depth $y_0'(y)$, and in the lower layer (region 2) we find that this places the current electrodes below the position y (that is, $y_0'(y) > y$). Fig. 6*b* shows this optimum depth $y_0'(y)$, given as $\{y_0'(y)-y\}/h$, as a function of y/h for the particular conditions of the figure. The function for the envelope current density can be written $J_e(y)$ and we must have

$$J_e(y) = J_z(y;\, y_0'(y)) \,. \tag{6}$$

Specific expressions for $y_0'(y)$ and $J_e(y)$ cannot usually be obtained, and these functions are determined numerically in the required cases.

The current density distribution for electrodes at large depths ($y'/h \gg 1$) approaches a fixed form shown by the dot–dash curve in Fig. 6*a*; the maximum current density approaches the homogeneous value

$$J_m = I/2\pi z'^2 .$$

We note particularly that the envelope curve shows that the current density below, but close to, the interface can never be increased to near this homogeneous value, since there is always a region of depleted current density there no matter how close to the interface the electrodes are placed.

We also note that the current density distribution for electrodes sited at $y'_0(y)$ does not peak at y (cf. Fig. 6*a*) but at a depth $y_p(y)$, say. We can determine the position and magnitude of this peak by noting the result (proved in Appendix 2) that if current electrodes are placed at y'_c, say, then the maximum in the current density occurs at

$$y_m(y'_c) = y'_0(y'_c). \tag{7}$$

The function on the right-hand side here is the same function as that noted above for the optimum positioning of the electrodes and shown in Fig. 6*b*. The value of the peak current density is $J_z(y_m; y'_c)$ which, by equation (5), is equal to $J_z(y'_c; y_m)$, and this in turn, by equations (6) and (7), is the value of $J_e(y'_c)$, the envelope current density at the electrode depth. Thus to optimize the current density at y, the electrodes are placed at a depth $y'_0(y)$, the current density at y is $J_e(y)$, and the resultant current density distribution peaks at

$$y_p = y_m\big(y'_0(y)\big) \equiv y'_0\big(y'_0(y)\big), \tag{8}$$

with value $J_e\big(y'_0(y)\big)$, that is, the envelope value at the electrode position.

In the assessment, in a practical application, of the siting of the electrodes, current density curves such as those of Fig. 5 appropriate to the values of s, z' and y' are required. One can, of course, make a complete calculation of the curves but in many cases a quickly obtained approximation is adequate. A useful approximation of the current density curves can be produced from curves of the envelope function $J_e(y)$, the associated optimum-depth function $y'_0(y)$, the current density curve $J_z(y; h)$ for electrodes at the interface ($y' = h$) and the current density curve for electrodes at large depth.

The construction of the approximate current density distribution depends upon the results noted in the preceding paragraphs, and the graphical procedure is illustrated in Fig. 7. It is as follows: If the current electrodes are at depth y_1 then the current distribution peaks at y_2, touches the envelope curve at y_3 and meets the interface at $J_z(h; y_1)$. The current density at y_2 is the envelope value at y_1 and the distribution below this peak (i.e. for $y > y_2$) has the homogeneous form (the dot–dash curve H in Fig. 7). The current density curve meets the interface at $J_z(h; y_1)$ and since, by equation (5), this is equal to $J_z(y_1; h)$ it can be constructed from the given distribution $J_z(y; h)$ as shown. The interface point, envelope point, peak point and the shape beyond the peak is sufficient information for an excellent approximation to the current density curve for electrodes at y_1 to be drawn.

Finally, in this section, we note that consideration of the optimum siting of electrode positions can arise when the potential electrodes are set downhole. With a fixed target depth the objective is to place the potential electrodes such that $\Delta\phi_d$ is maximized. We have already shown that the distribution of $\Delta\phi_d$ downhole has the same form as the current density distribution (i.e. except for the interface discontinuity discussed in Section 4, Fig. 5 applies equally well to potentials $\Delta\phi_d$); thus the whole of the discussion of envelopes, electrode placement for maximization and construction of the approximate distributions on the y axis, carried through for the current density, can be interpreted immediately in terms of potentials measured by downhole electrodes.

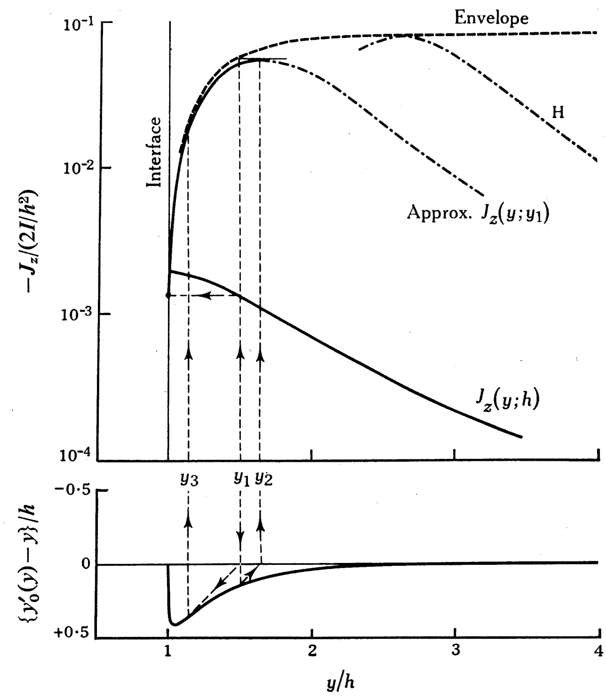

Fig. 7. Illustrating the construction of the approximate current density profile for electrodes at depth y_1 (under the conditions $s = 0{\cdot}01$, $z'/h = 1$). The curve for $J_z(y;y_1)$ peaks at y_2, touches the envelope at y_3 and meets the interface at $J_z(y_1;h)$ (see text). Note that to a good approximation the curve $J_z(y;h)$ versus y has the same shape as curve H, the homogeneous form ($y_1 \gg h$).

6. Reciprocity Relationships

In Section 4 we noted that the expressions for $J_z(y;y')$ and $\Delta\phi_d(y;b)$ had the same form. This identical form is a special case of more general results arising from the fact, noted in Section 2, that the Green's function $G(\boldsymbol{x};\boldsymbol{x}')$ is symmetric in its arguments $\boldsymbol{x}$ and $\boldsymbol{x}'$. Two such theorems which are useful in this problem are given below.

Theorem 1. Suppose that a monopole current source of unit strength at $\boldsymbol{x}'$ produces a current density $\boldsymbol{j}(\boldsymbol{x};\boldsymbol{x}')$ at position $\boldsymbol{x}$. Then a current dipole of moment

p at x produces a potential

$$\phi_d(x';x) = -p.j(x;x')/\sigma(x) \tag{9}$$

at position x'.

The relationship (9) is the primary one here and its proof is the development of equation (A4) in Appendix 1. An example of its application is the case of electrodes at x_1 and x_2 and a target at position x_0. If the electrodes are used as current electrodes with currents I_0 and $-I_0$ respectively, the current density at x_0 is

$$J(x_0;x_1,x_2) = I_0 j(x_0;x_1) - I_0 j(x_0;x_2). \tag{10}$$

If there is a current dipole of moment p at x_0, the potential difference between x_1 and x_2 is

$$\Delta\phi_d(x_1,x_2;x_0) = \phi_d(x_1;x_0) - \phi_d(x_2;x_0). \tag{11}$$

With the use of equations (9) and (10) this becomes

$$\Delta\phi_d(x_1,x_2;x_0) = -p.J(x_0;x_1,x_2)/I_0\,\sigma(x_0), \tag{12}$$

and when p is parallel to J

$$\Delta\phi_d(x_1,x_2;x_0)/p = -J(x_0;x_1,x_2)/I_0\,\sigma(x_0). \tag{13}$$

This result shows in general the identical mathematical dependence upon x_1 and x_2 of: (i) the current density at x_0 due to currents I_0 and $-I_0$ at the electrodes and (ii) the potential difference between x_1 and x_2 due to a dipole at x_0. In particular, positions of x_1, x_2 which maximize J at x_0 are those necessary to maximize $\Delta\phi_d$ with a dipole at x_0. The equivalence of the expressions for J_z and $\Delta\phi_d$ noted in Section 4 and used in this paper is a special consequence of this result and theorem 2(iii) noted below.

Theorem 2. If $j_{\parallel}(x;x')$ is the current density parallel to the surface at $x = (x,y,z)$ due to a unit source at $x' = (x',y',z')$ then $j_{\parallel}$ has the following properties under interchange of coordinates:

(i) interchange of x and x' reverses j_x,

$$j_x(x,y,z;x',y',z') = -j_x(x',y,z;x,y',z');$$

(ii) interchange of z and z' reverses j_z

$$j_z(x,y,z;x',y',z') = -j_z(x,y,z';x',y',z);$$

(iii) interchange of y and y' maintains the direction of $j_{\parallel}$ with

$$\sigma(y')j_{\parallel}(x,y,z;x',y',z') = \sigma(y)j_{\parallel}(x,y',z;x',y,z');$$

(iv) interchange of source point x' and field point x yields

$$\sigma(x')j_{\parallel}(x;x') = -\sigma(x)j_{\parallel}(x';x).$$

The results (i)–(iv) are a consequence of the reciprocity of $G(\boldsymbol{x};\boldsymbol{x}')$ and the planar geometry. From these factors we have

$$G(\boldsymbol{x};\boldsymbol{x}') = F\{(x-x')^2+(z-z')^2, y, y'\} = F\{(x'-x)^2+(z'-z)^2, y', y\} = G(\boldsymbol{x}';\boldsymbol{x}), \tag{14}$$

and (i)–(iv) follow from the relation (14) and $\boldsymbol{j} = -\sigma\nabla G$. The results (i) and (ii) are also obvious from the geometry, while (iv) follows from the first three results or may be obtained directly. The relation (14) and hence the results (i)–(iv) also apply to the general case of σ a function of y only. The relation (5) used extensively in the discussion of envelopes and maximization in Section 5 is a particular application of (iii) with $\sigma(y) = \sigma(y')$.

7. Frequency-domain IP and Time-domain IP

In practice time-domain IP and frequency-domain IP measurement techniques are used rather than the direct current (DC) technique for which our calculations have been made so far in this paper. In this section we relate our previous results to the more commonly measured quantities of these domains and show that the same reductions (and improvements) apply to them.

Our analysis here involves the inclusion of frequency dependence. The basis is the widely used method of Siegel (1959) of modelling the IP sources by regions of different conductivity σ_p which, in a polarizable material, is a function of the angular frequency ω. Following our DC analysis, a small polarizable sphere of volume V in a medium of conductivity σ_m can then be replaced by a frequency-dependent current dipole at the centre of the sphere with a moment $\boldsymbol{p}$ given by

$$\boldsymbol{p} = -k(\omega)\,\boldsymbol{J}, \qquad \text{with} \qquad k(\omega) = 3V(\sigma_m-\sigma_p)/(2\sigma_m+\sigma_p), \tag{15}$$

when the applied current density is $\boldsymbol{J}$. The frequency-dependent conductivity of the IP source, $\sigma_p(\omega)$, may be complex, thus giving a phase relationship between current and potential; the background conductivity σ_m is considered to be independent of frequency.

In frequency-domain IP, the system is excited by the same current first at ω_1 then at ω_2 and the corresponding potentials $\phi(\omega_1)$ and $\phi(\omega_2)$ are measured at the potential electrodes. The frequency-effect parameter FE, defined by

$$FE = \{\phi(\omega_1)-\phi(\omega_2)\}/\tfrac{1}{2}\{\phi(\omega_1)+\phi(\omega_2)\}, \tag{16}$$

is used as a measure of the IP effect. To relate this FE to the present work we note that a monopole source of strength $I(\omega)$ placed at $\boldsymbol{x}'$ produces a potential

$$I(\omega)\,G(\boldsymbol{x};\boldsymbol{x}')$$

at $\boldsymbol{x}$ (electromagnetic coupling effects can be ignored provided frequencies are sufficiently low). This results in a source dipole at the target point $\boldsymbol{x}_s$ of moment

$$\boldsymbol{p} = -k(\omega)\,\boldsymbol{J}(\boldsymbol{x}_s;\boldsymbol{x}') = +k(\omega)\,\sigma_m I(\omega)\,\partial G(\boldsymbol{x}_s;\boldsymbol{x}')/\partial \boldsymbol{x}_s. \tag{17}$$

From equation (9) the resultant potential at a measuring point x is given by

$$\begin{aligned}\phi(\omega) &= I(\omega)\,G(x;x') + p(\omega).\{\partial G(x;x_s)/\partial x_s\} \\ &= I(\omega)\big[G(x;x') - \{k(\omega)/\sigma_m\}\,j(x_s;x').j(x_s;x)\big].\end{aligned} \tag{18}$$

Consequently, with $I(\omega_1) = I(\omega_2) = I$, we have

$$FE = \frac{k(\omega_2)-k(\omega_1)}{\sigma_m}\left(\frac{j(x_s;x').j(x_s;x)}{G(x;x')}\right). \tag{19}$$

When the IP source is in the lower region, the effective conductivity $\sigma_p(\omega)$ and $k(\omega)$ are not likely to be changed by the overburden. Thus FE in the presence of overburden is changed by a factor

$$\left(\frac{j(x_s;x').j(x_s;x)}{G(x;x')}\right)_{\sigma_1,\sigma_2}\Bigg/\left(\frac{j(x_s;x').j(x_s;x)}{G(x;x')}\right)_{\sigma_2,\sigma_2}. \tag{20}$$

This factor can be calculated readily from our DC formulae, and its relationship to our present calculations is discussed below.

In time-domain IP, the decaying signal voltage due to IP sources is observed after the termination of a steady excitation current I applied at x' from $t = 0$ to t_0. The potential at x in this case is obtained by Fourier analysis, treating the applied signal as having a continuous distribution $i(\omega)\,\mathrm{d}\omega$ in the angular-frequency interval ω to $\omega+\mathrm{d}\omega$ and summing the effects of these currents by evaluating the potential

$$\Phi(t) = \int_{-\infty}^{+\infty} \phi(\omega)\exp(\mathrm{i}\omega t)\,\mathrm{d}\omega, \tag{21}$$

in which $\phi(\omega)$ is the monochromatic response given by equation (18) with $I(\omega)$ replaced by $i(\omega)$. Carrying out the analysis gives

$$\begin{aligned}\Phi(t) &= I\,G(x;x')\{U(t)-U(t-t_0)\} \\ &\quad -\{K(t)\,U(t) - K(t-t_0)\,U(t-t_0)\}\{j(x_s;x).j(x_s;x')\}/\sigma_m,\end{aligned} \tag{22}$$

with

$$K(t) = (2\pi\mathrm{i})^{-1}\int_{-\infty+ic}^{+\infty+ic} \omega^{-1}\,k(\omega)\exp(\mathrm{i}\omega t)\,\mathrm{d}\omega \tag{23}$$

and $U(t)$ the step function: $U(t) = 0,\ t < 0;\ U(t) = 1,\ t > 0$.

The second line of equation (22) gives the signal rise after switching on at $t = 0$ and the signal decay after switching off at $t = t_0$ due to the IP sources. It can be evaluated given $k(\omega)$. However, for our present purposes this evaluation is not necessary, we simply note again that $k(\omega)$ is the same with or without overburden and thus so is $K(t)$. Consequently the signal at all times in the decay phase is changed by the factor

$$\big(j(x_s;x).j(x_s;x')\big)_{\sigma_1,\sigma_2}/\big(j(x_s;x).j(x_s;x')\big)_{\sigma_2,\sigma_2}, \tag{24}$$

which is the same factor as in the DC case. Thus our DC comparisons are immediately relevant whether one is interested in the amplitude immediately after switching off at $t = t_0$ or in the integrated response.

The factor (24) is roughly proportional to s^2 and represents an attenuation of the signal in the presence of overburden of higher conductivity than the host rock ($s = \sigma_2/\sigma_1 < 1$). We note here that the factor (20) for the *FE* differs from (24) by a factor

$$(G(x;x'))_{\sigma_2,\sigma_2}/(G(x;x'))_{\sigma_1,\sigma_2},$$

which is $\sim s^{-1}$. Hence the factor for *FE* is roughly proportional to s rather than s^2. Thus it may appear that *FE* is a better measure to use in field surveys. This is misleading and is a consequence of the normalization introduced by the division by $\frac{1}{2}\{\phi(\omega_1)+\phi(\omega_2)\}$ which is essentially the voltage at the measuring site without IP signal and is proportional to s. The same *apparent* improvement can be obtained for time-domain studies by normalizing with the potential prior to t_0. The important point here is that the signals are attenuated by the overburden by the factor (24) *in each case* and it is necessary to be able to detect them in the presence of background potentials. No artificial normalization will change this fact.

8. Discussion and Conclusions

We have used a very simple model here to demonstrate quantitatively the effects of placing current and potential electrodes below the surface in IP surveys in locations with a highly conducting overburden layer. In practice we envisage the electrodes being placed down boreholes already existing or specially drilled. It is evident from the figures (e.g. Figs 4 and 5) that the substantial shielding of the ore body by the overburden can be overcome by going downhole. In general, however, little improvement is obtained until the current or potential electrodes are placed substantially below the overburden–host-rock interface.

In the case of the particular geometry used here for illustration we have shown the spatial distributions of current and potential. A typical practical case may have overburden of depth h $\sim$100 times as conductive as the host rock, an IP target at depth $\sim 2h$ below the surface, and potential and current electrodes at separations of h and $2h$ respectively. With electrodes on the surface the overburden reduces the IP signal voltage to about 1/1000 of that of the homogeneous case. This factor is changed to 1/2 by placing the current electrodes at depths of $\sim 1{\cdot}7h$, and so, for practical purposes, the severe attenuation is completely overcome.

We have also taken up the question of positioning of the electrodes for maximum excitation of the target IP source and maximization of the signal potential received. Although the simple target to current-electrode geometry assumed will not generally prevail in practice, the concepts introduced here will be useful in more general cases. The main conclusion from the maximization study is that there is a blind zone just beneath the interface. This is of major importance in exploration surveys in Australia, for it means that targets that are in this zone are shielded by the overburden even if the electrodes are placed downhole.

Either current electrodes, potential electrodes, or both may be placed downhole; there will be practical difficulties with both in the same hole and a combination of downhole current electrodes and surface potential electrodes may be most useful.

We note that the placement of potential electrodes downhole restricts the range of mapping one has available, since essentially one is replacing mapping in the surface plane with mapping on a vertical line (or lines).

The signal potentials given have been determined for direct currents and potentials. We have shown that they are directly applicable to the time-domain and frequency-domain signal potentials measured in practical surveys.

Finally we remark that the model assumed here has been a simple one, assuming a small target source. With an extended source the details will be different but we expect that the considerable shielding of the overburden layer will be overcome again if electrodes can be sited below the interface.

Acknowledgments

This work was suggested to us by Dr K. G. McCracken and we thank him and Mr R. L. Drinkrow, both of the Division of Mineral Physics, CSIRO, for many vigorous and useful discussions on this work. Funds were provided by CSIRO for the computation work necessary in this study.

References

Gleeson, L. J., and Thio, Y.-C. (1973). CSIRO Minerals Research Laboratory Investigation Rep. No. 99.

Hansen, D. A., *et al.* (1967). 'Mining Geophysics', Vol. 2 (Society of Exploration Geophysicists: Toronto).

Hummel, J. N. (1932). *AIME Geophys. Prospect.* **97**, 392.

Morse, P. M., and Feshbach, H. (1953). 'Methods of Theoretical Physics', Part I, Ch. 7 (McGraw–Hill: New York).

Parasinis, D. S. (1966). 'Mining Geophysics' (Elsevier: Amsterdam).

Siegel, H. O. (1959). *Geophysics* **14**, 547.

Appendix 1. Green's Function

With a homogeneous medium, the Green's function of equation (1) in Section 2 is simply $G(\boldsymbol{x};\boldsymbol{x}') = (4\pi\sigma\,|\,\boldsymbol{x}-\boldsymbol{x}'\,|)^{-1}$. For the stratified geometry of Fig. 1, the Green's function can be constructed from the original source together with an infinite set of images of appropriate strength. For a source point at $\boldsymbol{x}'$ and an overburden thickness h, the images are located at the positions:

$$\hat{\boldsymbol{x}}'(n) = \boldsymbol{x}'+2nh\boldsymbol{k}, \qquad n = \pm 1, \pm 2, \dots,$$

$$\tilde{\boldsymbol{x}}'(n) = \boldsymbol{x}'-2\{nh+(\boldsymbol{x}'-\boldsymbol{g}).\boldsymbol{k}\}\boldsymbol{k}, \qquad n = 0, \pm 1, \pm 2, \dots.$$

In these expressions $\boldsymbol{g}$ is the position vector of any point on the ground surface and $\boldsymbol{k}$ is a downward unit vector normal to that surface.

Denoting the overburden layer as region R_1 and the lower layer as region R_2, the Green's function $G(\boldsymbol{x};\boldsymbol{x}')$ at $\boldsymbol{x}$ for the source at $\boldsymbol{x}'$ is given by

$$4\pi\,\sigma(\boldsymbol{x})\,G(\boldsymbol{x};\boldsymbol{x}')$$

$$= \sum_{n=-\infty}^{\infty} p_{12}^{|n|}\{|\boldsymbol{x}-\hat{\boldsymbol{x}}'(n)|^{-1}+|\boldsymbol{x}-\tilde{\boldsymbol{x}}'(n)|^{-1}\}, \qquad \boldsymbol{x}\in R_1,\ \boldsymbol{x}'\in R_1; \quad \text{(A1a)}$$

$$= (1-p_{12})\sum_{n=0}^{\infty} p_{12}^{n}\{|\boldsymbol{x}-\hat{\boldsymbol{x}}'(n)|^{-1}+|\boldsymbol{x}-\tilde{\boldsymbol{x}}'(n)|^{-1}\}, \qquad \boldsymbol{x}\in R_2,\ \boldsymbol{x}'\in R_1; \quad \text{(A1b)}$$

$$= (1+p_{12})\sum_{n=0}^{\infty} p_{12}^{n}\{|\boldsymbol{x}-\hat{\boldsymbol{x}}'(n)|^{-1}+|\boldsymbol{x}-\tilde{\boldsymbol{x}}'(n)|^{-1}\}, \qquad \boldsymbol{x}\in R_1,\ \boldsymbol{x}'\in R_2; \quad \text{(A1c)}$$

$$= |\boldsymbol{x}-\boldsymbol{x}'|^{-1}-p_{12}|\boldsymbol{x}-\tilde{\boldsymbol{x}}'(-1)|^{-1}$$

$$+(1-p_{12}^2)\sum_{n=0}^{\infty} p_{12}^{n}|\boldsymbol{x}-\tilde{\boldsymbol{x}}'(n)|^{-1}, \qquad \boldsymbol{x}\in R_2,\ \boldsymbol{x}'\in R_2. \quad \text{(A1d)}$$

Here $\sigma(\boldsymbol{x})$ is the conductivity at position $\boldsymbol{x}$, with the value σ_1 for $\boldsymbol{x}\in R_1$ and σ_2 for $\boldsymbol{x}\in R_2$, and

$$p_{12} = (\sigma_1-\sigma_2)/(\sigma_1+\sigma_2)$$

is the reflection coefficient at the interface. Each term represents a contribution from an image point. The expression (A1a) is for the case of both electrodes in the overburden or upper layer, and the other cases can be identified similarly. The reciprocity between $\boldsymbol{x}$ and $\boldsymbol{x}'$ in equations (A1) is apparent if we note the relationships

$$|\boldsymbol{x}-\hat{\boldsymbol{x}}'(n)| = |\boldsymbol{x}'-\hat{\boldsymbol{x}}(-n)|, \qquad |\boldsymbol{x}-\tilde{\boldsymbol{x}}'(n)| = |\boldsymbol{x}'-\tilde{\boldsymbol{x}}(n)|,$$

which are a property of the circumflex ($\hat{\boldsymbol{x}}'$) and tilde ($\tilde{\boldsymbol{x}}'$) image operators.

We obtained the solutions (A1) using image techniques similar to those employed in potential theory in electrostatics with dielectric layers. Subsequently we found the results to be well established in the literature (e.g. Hummel 1932) and also developed alternatively by Hansen *et al.* (1967).

The current density at $\boldsymbol{x}$ due to a unit monopole at $\boldsymbol{x}'$ is obtained from

$$\boldsymbol{j}(\boldsymbol{x};\boldsymbol{x}') = -\sigma(\boldsymbol{x})\,\partial G(\boldsymbol{x};\boldsymbol{x}')/\partial\boldsymbol{x} \quad \text{(A2)}$$

and given explicitly in this case by differentiating the expressions (A1):

$$4\pi\,\boldsymbol{j}(\boldsymbol{x};\boldsymbol{x}')$$

$$= \sum_{n=-\infty}^{\infty} p_{12}^{|n|}\{|\boldsymbol{x}-\hat{\boldsymbol{x}}'(n)|^{-3}(\boldsymbol{x}-\hat{\boldsymbol{x}}'(n))$$

$$+|\boldsymbol{x}-\tilde{\boldsymbol{x}}'(n)|^{-3}(\boldsymbol{x}-\tilde{\boldsymbol{x}}'(n))\}, \qquad \boldsymbol{x}\in R_1,\ \boldsymbol{x}'\in R_1; \quad \text{(A3a)}$$

$$= (1-p_{12})\sum_{n=0}^{\infty} p_{12}^{n}\{|\boldsymbol{x}-\hat{\boldsymbol{x}}'(-n)|^{-3}(\boldsymbol{x}-\hat{\boldsymbol{x}}'(-n))$$

$$+|\boldsymbol{x}-\tilde{\boldsymbol{x}}'(n)|^{-3}(\boldsymbol{x}-\tilde{\boldsymbol{x}}'(n))\}, \qquad \boldsymbol{x}\in R_2,\ \boldsymbol{x}'\in R_1; \quad \text{(A3b)}$$

$$= (1+p_{12}) \sum_{n=0}^{\infty} p_{12}^{n}\{|x-\hat{x}'(n)|^{-3}(x-\hat{x}'(n))$$

$$+|x-\tilde{x}'(n)|^{-3}(x-\tilde{x}'(n))\}, \qquad x \in R_1,\ x' \in R_2; \quad \text{(A3c)}$$

$$= |x-x'|^{-3}(x-x') - p_{12}|x-\tilde{x}'(-1)|^{-3}(x-\tilde{x}'(-1))$$

$$+(1-p_{12}^2) \sum_{n=0}^{\infty} p_{12}^{n}|x-\tilde{x}'(n)|^{-3}(x-\tilde{x}'(n)), \qquad x \in R_2,\ x' \in R_2. \quad \text{(A3d)}$$

The potential at x due to a current dipole of moment p' sited at x' is

$$\begin{aligned} \phi_d(x;x') &= p'.\{\partial G(x;x')/\partial x'\}, \\ &= p'.\{\partial G(x';x)/\partial x'\}, \\ &= -p'.\{j(x';x)/\sigma(x')\}, \end{aligned} \quad \text{(A4)}$$

the last step following from equation (A2). Since the relation (A4) involves $j(x;x')$ which is given by the series (A3), we may again use those series to evaluate $\phi_d(x;x')$.

Appendix 2. Maximization of Current Density $J_z(y;y')$

With the geometry of this problem, the current density $J_z(y;y')$ at a depth y on the y axis is given explicitly by equation (3) in Section 3. The function $y_0'(y)$ giving the value of y' which maximizes $J_z(y;y')$ at fixed y is given implicitly by each of the equations

$$\partial J_z(y;y_0')/\partial y_0' = 0, \qquad \partial J_z(y_0';y)/\partial y_0' = 0. \quad \text{(A5a, b)}$$

The second of these follows from the first on noting $J_z(y;y') = J_z(y';y)$. With y' fixed, the current density peaks at $y_m(y')$ given implicitly by

$$\partial J_z(y_m;y')/\partial y_m = 0. \quad \text{(A6)}$$

Except for notation, equations (A6) and (A5b) are identical, and hence

$$y_m(\eta) = y_0'(\eta), \quad \text{(A7)}$$

as noted in equation (7) of Section 5.

Manuscript received 13 March 1975